Check for updates

Enhanced magnetic susceptibility in Ti₃C₂Tₓ MXene with Co and Ni incorporation†

Yizhou Yang, [ID] ‡[a] Mark Anayee, [ID] ‡[a,b] Ajith Pattammattel, [ID] [c]
Mikhail Shekhirev, [ID] [a,b] Ruocun (John) Wang, [ID] [a,b] Xiaojing Huang, [ID] [c]
Yong S. Chu, [ID] [c] Yury Gogotsi [ID] [a,b] and Steven J. May [ID] *[a]

Magnetic nanomaterials are sought to provide new functionalities for applications ranging from information processing and storage to energy generation and biomedical imaging. MXenes are a rapidly growing family of two-dimensional transition metal carbides and nitrides with versatile chemical and structural diversity, resulting in a variety of interesting electronic and optical properties. However, strategies for producing MXenes with tailored magnetic responses remain underdeveloped and challenging. Herein, we incorporate elemental Ni and Co into Ti₃C₂Tₓ MXene by mixing with dilute metal chloride solutions. We achieve a uniform distribution of Ni and Co, confirmed by X-ray fluorescence (XRF) mapping with nanometer resolution, with Ni and Co concentrations of approximately 2 and 7 at% relative to the Ti concentration. The magnetic susceptibility of these Ni- and Co-incorporated Ti₃C₂Tₓ MXenes is one to two orders of magnitude larger than pristine Ti₃C₂Tₓ, illustrating the potential for dilute metal incorporation to enhance linear magnetic responses at room temperature.

Introduction

MXenes encompass a rapidly growing and diverse family of two-dimensional (2D) materials, represented by the $M_{n+1}X_nT_x$ formula, where M is one or more early transition metals, X is carbon and/or nitrogen, T are surface terminations (including –O, –OH, halogens, and chalcogens), and n ranges from 1–4.[1–4] MXenes present a unique combination of properties that render them promising materials for applications such as electromagnetic interference shielding, implantable electrodes, and pseudocapacitive energy storage enabled by their large electronic conductivity and surface redox activity. Moreover, the hydrophilic surfaces of O- and OH-terminated MXenes allow for easy processing and device fabrication.[4] However, the ability to tailor the magnetic properties of MXenes is less-understood and lags behind activities focused on electrochemical, electronic, or optical behavior. The development of MXenes with robust magnetic responses, through

either enhancing their linear susceptibility in paramagnetic phases or realizing long-range magnetically ordered states, could enable the use of MXenes in magnetic technologies.[5]

The search for MXenes with magnetic ordering has been the subject of extensive computational studies, yielding predictions of both ferromagnetic and antiferromagnetic phases. Density functional theory (DFT) calculations predict that magnetic behavior can be tuned intrinsically by changing the M-site metal,[6–11] the surface termination species,[7,10,12–17] and extrinsically by applying strains.[18–20] The ability to test these computational predictions rests on the synthetic feasibility of the targeted MXene. MXenes are typically derived by selective etching of the A element (*e.g.*, Al) from layered MAX phase precursors,[21,22] represented by $M_{n+1}AX_n$. For example, Cr_2CT_x MXenes have been predicted to exhibit ordered magnetic states,[23–26] and in principle, these materials could be derived from parent MAX phases, such as Cr_2AlC and Cr_2GeC.[27] However, synthesis of the corresponding Cr_2CT_x MXene is challenging, has only recently been reported, and needs to be further confirmed.[28] Another Cr-based MXene that has been predicted to host magnetic ordering is $Cr_2TiC_2T_x$.[10,11,14,29] This material was successfully synthesized and found to exhibit a spin-freezing transition temperature near 30 K, indicative of local magnetic interactions but lacking an ordered magnetic state.[30]

An alternative approach for controlling magnetic behavior in MXenes is incorporating secondary phase particles into paramagnetic MXenes, such as the prototypical Ti₃C₂Tₓ. Along

[a]Department of Materials Science and Engineering, Drexel University, Philadelphia, Pennsylvania 19014, USA. E-mail: smay@drexel.edu
[b]A.J. Drexel Nanomaterials Institute, Drexel University, Philadelphia, Pennsylvania 19104, USA
[c]Brookhaven National Laboratory, National Synchrotron Light Source II, Upton, New York 11973, USA
†Electronic supplementary information (ESI) available. See DOI: https://doi.org/10.1039/d3nr05685f
‡These authors contributed equally to the work.

these lines, the synthesis of MXene-ferromagnetic nanoparticle composites has been widely studied as a route to engineer properties related to electromagnetic shielding.[31–35] One commonly used synthetic strategy is to employ metal chlorides mixed in a solution with MXenes as the precursors for the ferromagnetic second phase. For example, a wide range of morphologies have been realized in ferromagnetic Ni phases adhered to MXenes using $NiCl_2 \cdot 6H_2O$-containing solutions, including Ni chains or rods,[36,37] spherical particles,[38–42] and shells.[43] Similarly, $CoCl_2 \cdot 6H_2O$ has been utilized to create Co-based nanoparticles that bolster microwave absorption in MXene-based composites.[40,44] In these composites, clear ferromagnetic behavior is observed due to the non-MXene ferromagnetic secondary phase. A less-studied strategy for engineering magnetic responses is incorporating magnetically active ions in dilute concentrations into MXenes flakes without forming secondary phases, as dilute atomic concentrations of Ni and Co can impact electromagnetic wave absorption.[45,46] For example, dilute concentrations of Mn were incorporated into $Ti_3C_2T_x$ utilizing a solution of $Mn(CH_3COO)_2 \cdot 4H_2O$ dissolved in ethanol.[47] The resultant MXenes exhibited an increase in magnetic susceptibility compared to $Ti_3C_2T_x$ without inducing magnetic order. Ni atoms have also been incorporated into $Ti_3C_2T_x$ by immersing $Ti_3C_2T_x$ into a KOH solution containing $NiCl_2 \cdot 6H_2O$.[48] Multilayer powders of these Ni-$Ti_3C_2T_x$ were found to exhibit enhanced performance for microwave absorption applications, but the magnetic properties of the materials were not reported, nor was the nanoscale distribution of Ni atoms. Ni-intercalated $Mo_2TiC_2T_x$ has also been synthesized via mixing MXene ink with a $NiCl_2 \cdot 6H_2O$ solution, but the magnetic properties of these materials were not reported.[49] The limited reports of single-phase MXenes hosting magnetic elements such as Ni, Co, or Fe point to the need to better understand the magnetic responses of such materials.

In this work, we incorporated Ni and Co into delaminated $Ti_3C_2T_x$ MXene sheets by mixing with metal chloride solutions under conditions that do not result in the formation of ferromagnetic secondary phase particles. By using a low concentration of metal chloride solutions (<0.03 M), it was possible to prevent aggregation of the negatively charged MXenes sheets by self-assembly with the positively charged metal cations. We show that the incorporation of Ni and Co results in significant increases in room temperature magnetic susceptibility, presenting a promising strategy for modifying linear magnetic responses through dilute ion incorporation in single-phase MXenes.

Results and discussion

Delaminated d-$Ti_3C_2T_x$ MXene was prepared following standard procedures for MXene synthesis, as described in the Methods section. The incorporation of Ni and Co was realized by dissolving 0.2 g of $NiCl_2 \cdot 6H_2O$ and 0.156 g of anhydrous $CoCl_2$ in 35 mL of DI water, respectively. The salt solutions were added to 5 mL ($\sim$2 mg mL^{-1}) of d-$Ti_3C_2T_x$ dispersions and mixed for 15 min at room temperature. The resulting dispersions were washed with DI water through a series of centrifugation, mechanical shaking, and decantation cycles until the color became transparent. Free-standing $Ti_3C_2T_x$, Co-$Ti_3C_2T_x$ and Ni-$Ti_3C_2T_x$ films were successfully prepared from the MXene dispersions by vacuum-assisted filtration (Fig. 1). The cross-sectional scanning electron microscopy (SEM) micrographs of the free-standing films show the lamellar stacking of the MXene sheets before and after Ni and Co incor-

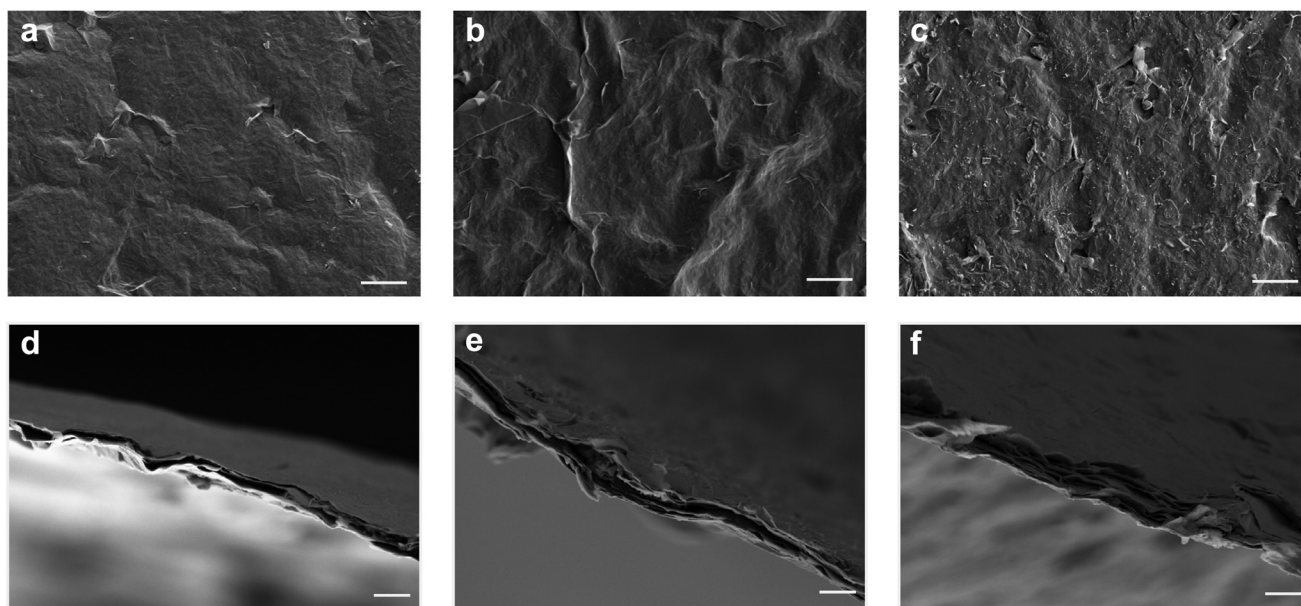**Fig. 1** Scanning electron microscopy (SEM) images of (a and d) pristine and (b and e) Co and (c and f) Ni incorporated $Ti_3C_2T_x$ MXene free-standing films showing the (top) surface and (bottom) cross-section. Scale bars are 5 μm for (a–c) and 2 μm for (d–f).

poration (Fig. 1d–f and Fig. S1†). The surface of the pristine MXene film is mostly smooth, with a few defects and titania crystals on the edges of MXene flakes indicative of oxidation and a few wrinkles and bumps indicative of the roughness of the filtration membrane (Fig. 1a and Fig. S1a†). After the incorporation of Co, the surface of the resulting film is similar to that of the pristine MXene (Fig. 1b and Fig. S1b†), while the

incorporation of Ni resulted in some wrinkling of the film surface (Fig. 1c and Fig. S1c†). The corresponding energy-dispersive X-ray spectroscopy (EDS) maps of the film surfaces indicate that both Co and Ni are uniformly dispersed throughout the films, although local areas with high Ni concentration exist correlated with areas of high Ti concentration, which suggests some local agglomeration of MXene sheets (Fig. S1†).

The ordered out-of-plane stacking of the MXene sheets in the free-standing films is further indicated by the 00l peaks in the X-ray diffraction (XRD) patterns at a standard Cu K$_\alpha$ X-ray energy (Fig. 2), where the 002 peak at 5.74° indicates that the interlayer spacing is 15.39 Å compared to the d-spacing of completely dried multilayer MXene powder of 15.3 Å. After the Co and Ni metal incorporation, the 002 peak does not shift significantly, appearing at 5.74° and 5.98°, respectively, which further suggests that there is no significant growth of salt crystals in between the MXene sheets. However, the 002 peak broadens where the FWHM increases from 0.48° to 1.06° and 1.70°, respectively. This broadening is likely due to local structural inhomogeneities from the presence of Co and Ni in between the MXene sheets or from stacking disorder induced by Ni/Co incorporation within the M-site of the MXenes. Moreover, no new peaks appear that would suggest the presence of salt crystals.

To better understand the uniformity and the amount of Co and Ni within the samples, X-ray fluorescence mapping with nanometer resolution (nano-XRF) was performed at the National Synchrotron Light Source II (NSLS-II) at the 3-ID Hard X-ray Nanoprobe (HXN) beamline.[50] MXene sheets were deposited onto a Si substrate from a colloidal aqueous dispersion, which aggregated once dried as opposed to forming a smooth layered morphology as in the vacuum-assisted filtration process (Fig. S2†). The corresponding nano-XRF maps
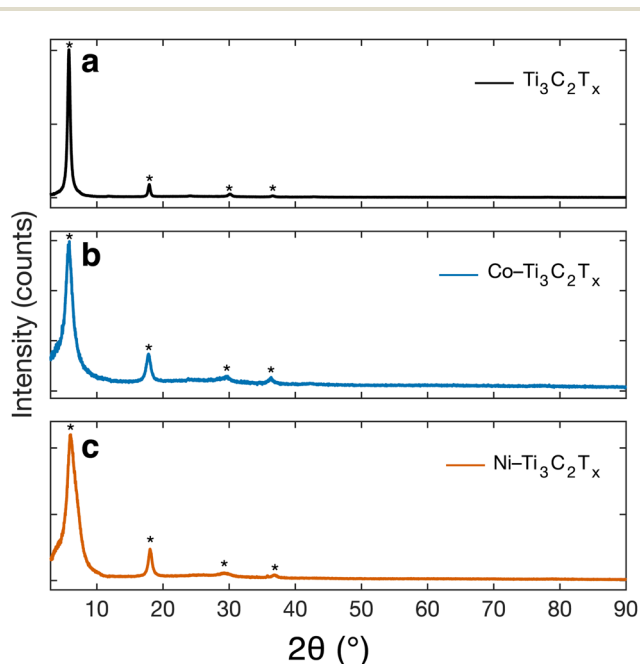
Fig. 2 X-ray diffraction (XRD) patterns of (a) pristine Ti$_3$C$_2$T$_x$ MXene, and after (b) Co and (c) Ni metal incorporation. The 00l peaks marked with asterisks (*) indicate the out-of-plane alignment of the MXene sheets in the free-standing films.
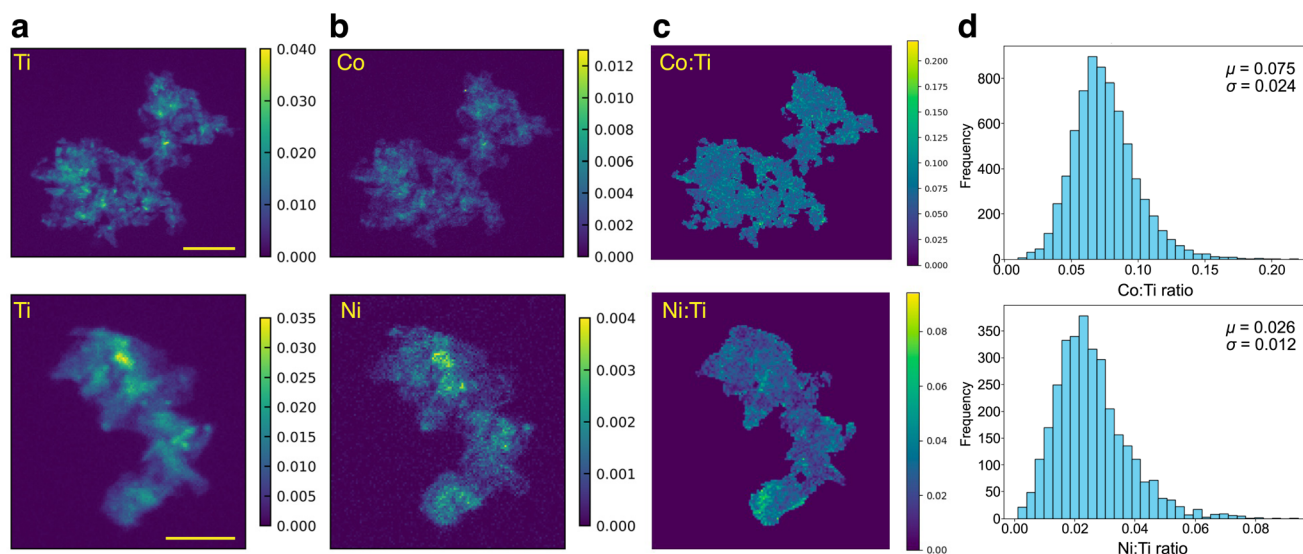
Fig. 3 X-ray fluorescence (XRF) mapping of MXene flakes drop-cast onto Si substrates. (a) Ti XRF map, (b) XRF map of the incorporated metal, and (c) intensity ratio of the incorporated metal and Ti. Scale bars are 2 μm. (d) Histograms showing the distribution of Co $vs.$ Ti and Ni $vs.$ Ti from the concentration values within each pixel in the XRF maps.

obtained with 50 nm step sizes show intensity distributions corresponding to the amount of each element present (Fig. 3a and b). In both Co- and Ni-$Ti_3C_2T_x$ samples, the distributions of Co and Ni follow that of Ti, suggesting that they are distributed throughout the MXene flakes instead of clustered as isolated particles. The variation of elemental intensity is due to the non-uniform deposition of the MXene sheets on the substrate. The uniform intensity across the maps correlating the Ti and Co/Ni distributions, after normalization by the X-ray fluorescence cross-sections (to obtain the number density of atoms per unit area),[51] further suggests the uniform distribution of Co and Ni across the flakes (Fig. 3c). The atomic ratios of Co to Ti and Ni to Ti, obtained from the overall integrated fluorescence intensity ratios after compensating for the corresponding XRF cross-sections, were found to be 0.075 and 0.026, respectively, based on the image histograms of the atomic ratios obtained from each pixel of the XRF maps (Fig. 3d). Analysis of six other clusters further supports the uniform distribution of Co and Ni, and lead to similar concentration values (Fig. S3 and S4†).

To investigate the coordination of the incorporated metals and their species, we probed the surface of free-standing MXene films using X-ray photoelectron spectroscopy (XPS) (Fig. 4). The Ti 2p core-level spectra indicate that the surface of all films is free of significant oxidation in the form of titania, assigned to the Ti 2$p_{3/2}$ component at ~459 eV (Fig. 4a–c). The Co 2p and Ni 2p core-level spectra indicate that both species appear predominantly as zero-valent metals, rather than metal chlorides (Fig. 4d and e), based on the binding energy of the major Co 2$p_{3/2}$ component at ~778 eV and the Ni 2$p_{3/2}$ component at ~853 eV.[52] Further, survey XPS spectra indicate no Cl present (Fig. S5†). The reduction of the metal chlorides suggests that the $Ti_3C_2T_x$ MXene was partially oxidized and acted as a reducing agent, evidenced by the slight increase in the oxide-related component in the Ti 2p spectra at ~459 eV. The negative values in the difference spectra of the Ti 2p region further support the shift in the spectra to higher binding energy and, therefore, slight oxidation (Fig. 4f). Moreover, as the concentration of the oxidizing salt (*e.g.*, $CoCl_2$) increased, the MXene was more oxidized, evidenced by the shift in the Ti 2p spectra to higher binding energy (Fig. S6a†), and the yield of reduction decreased, leaving behind some residual material (*e.g.*, CoO, Co_3O_4, *etc.*) (Fig. S6b†). A similar reduction of metals upon reaction with MXenes has been reported for U, Cd, Ru and Cu.[53–58]

To probe the influence of Ni and Co incorporation on the MXene structure and bonding, we performed Raman spectroscopy analysis (Fig. S7†). The resonant Raman peak, which is related to the coupling between the exciting Raman laser and the surface plasmon resonance in the MXene, shifts from ~127 cm^{-1} in pristine and Ni-incorporated MXene to ~125 cm^{-1} in Co-incorporated MXene, which suggests there are slight changes to the electronic structure of the material.[59] The out-of-plane A_{1g} (Ti, C, T_x) shifts from ~209 cm^{-1} in pristine MXene to ~210 and ~213 cm^{-1} in Ni and Co incorporated MXene, which indicates bond stiffening, possibly due to
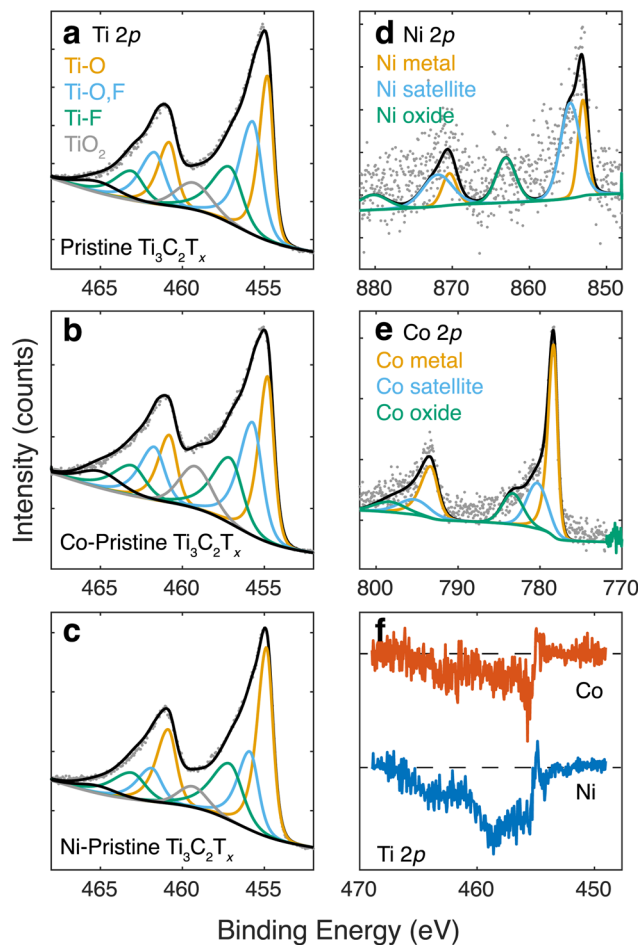

Fig. 4 X-ray photoelectron spectroscopy (XPS) of the (a–c) Ti 2p core-level from (a) pristine $Ti_3C_2T_x$ MXene, and after (b) Co and (c) Ni metal incorporation. Corresponding (d) Ni 2p and (e) Co 2p spectra. (f) Difference spectra, obtained by subtracting the metal-incorporated spectra from the pristine MXene spectra, for the Ti 2p core-level, indicating slight oxidation of the MXene during metal incorporation.

greater disorder in layer stacking and the presence of metal atoms near the MXene surface.[59] However, the A_{1g} (C) at ~734 cm^{-1}, E_g (C) at ~600 cm^{-1}, and the E_g (T_x) modes at ~290 and ~370 cm^{-1} appear unaffected by the metal incorporation. Moreover, no other species were detected in the Raman spectra, despite the high sensitivity of Raman spectroscopy to various impurities in MXene samples, such as nano-crystalline titania in $Ti_3C_2T_x$.

Aside from changes to the structure and chemistry, the slight increase in the Ti oxidation state has a relatively minimal impact on electronic conductivity. For example, the temperature-dependent resistivity measurements exhibit similar shapes with similar values for $\Delta\rho/\Delta T$ of 0.76, 1.2, and 0.85 μΩ cm K^{-1}, and room temperature resistivity values of ~0.96, 0.73, and 1.53 mΩ cm, for pristine, Co and Ni incorporated samples, respectively (Fig. S8†). Thus, the resistivity in Ni-$Ti_3C_2T_x$ is increased by a factor of approximately 1.5 compared to $Ti_3C_2T_x$.

The magnetic properties of the MXenes were investigated using DC magnetometry (Fig. 5). The field-dependent magnetization (M vs. H) curves at different temperatures indicate that pristine $Ti_3C_2T_x$ MXene is paramagnetic as it exhibits a linear relationship, with very low magnetization of $\sim 4 \times 10^{-4}$ emu g^{-1} at 300 K and 1.5×10^{-3} emu g^{-1} at 10 K under an applied field of 0.2 T (Fig. 5a). The M vs. H curves for Co and Ni incorporated $Ti_3C_2T_x$ MXene exhibit non-linear behavior below 50 K and 20 K (Fig. 5b and c), respectively, that indicate deviations from simple paramagnetism at low temperature, which can be fit with the Langevin function (Fig. S9 and Table S1†).[60–62] Importantly, the incorporation of these magnetically active transition metals into $Ti_3C_2T_x$ MXene samples leads to a significant increase in the room temperature magnetization with the susceptibility increasing from 2.0×10^{-7} emu g^{-1} Oe^{-1} for $Ti_3C_2T_x$, to 1.1×10^{-5} emu g^{-1} Oe^{-1} and 2.3×10^{-6} emu g^{-1} Oe^{-1} for Co- and Ni-incorporated $Ti_3C_2T_x$ (Fig. 5d).

For both, Co- and Ni-incorporated samples, the temperature-dependent magnetization (M vs. T) curves show that while there is a low-temperature upturn in magnetization, there is no evidence of a ferromagnetic or antiferromagnetic transition (Fig. 5e and f). The M vs. T curves for the chloride salts indicate that $CoCl_2$ exhibits a maximum in magnetization at 15.5 K, associated with an antiferromagnetic transition. The magnetization data from Co-$Ti_3C_2T_x$ does not exhibit a local maximum or anomaly near 15.5 K, providing further evidence that the MXene samples do not contain residual metal chloride salts. By comparing the magnetization values between the Co and Ni-incorporated MXene samples and the respective salts, we estimate it would require 10 wt% of salt incorporated in the sample to induce the change in the magnetization herein measured in the MXenes (Fig. 5e and f). Such a significant mass fraction of a secondary phase would be detectable by one of the characterization techniques presented earlier. The difference in the magnetic behavior observed for the salt and MXene sample, along with the large increase in magnetic susceptibility despite the low concentration of incorporated transition metal atoms, further support that the magnetization enhancement originates from a relatively uniform distribution of dilute Ni and Co atoms, rather than the presence of residual salt impurities. While this work establishes the general feasibility and utility of incorporating dilute concentrations of magnetic metal atoms in MXenes, future efforts are needed to understand the location of these atoms within or on the surface of MXenes and the upper limits to the Ni and Co concentrations that can be incorporated without the formation of ferromagnetic non-MXene secondary phases. Atomically resolved scanning transmission electron microscopy coupled with electron energy loss spectroscopy would be especially helpful in understanding whether the magnetic elements are
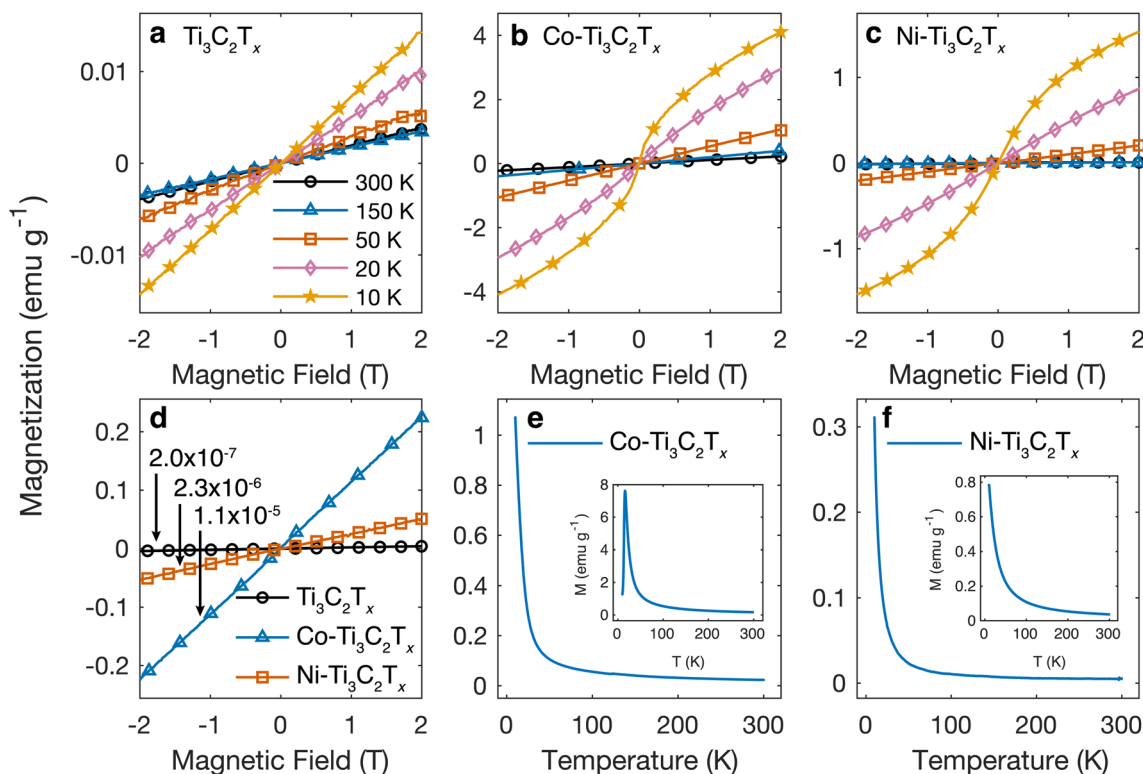

Fig. 5 (a–c) Field-dependent magnetization curves at different temperatures for (a) pristine $Ti_3C_2T_x$ and (b) Co- and (c) Ni-incorporated $Ti_3C_2T_x$. (d) Field-dependent magnetization curves at room temperature for $Ti_3C_2T_x$ MXene before and after metal incorporation. The magnetic susceptibility is indicated in terms of emu g^{-1} Oe^{-1}. (e and f) Temperature-dependent magnetization curves for (e) Co-$Ti_3C_2T_x$ and (f) Ni-$Ti_3C_2T_x$ at an applied field of 0.2 T. The insets are the temperature-dependent magnetization curves for $CoCl_2$ and $NiCl_2$ salt powders.

incorporated within Ti vacancies or other defect sites in the MXenes.

Conclusions

In summary, we demonstrated a method to incorporate a secondary metal element into delaminated $Ti_3C_2T_x$ MXene. While only Co and Ni are reported in this work, we anticipate that other transition metal elements with magnetic activity can also be incorporated into $Ti_3C_2T_x$ and other MXenes by mixing MXene dispersions with salt solutions at low concentrations to prevent significant oxidation of the MXene and neutralizing the negative surface charge of the MXene and cause agglomeration. Further, this work provides evidence that $Ti_3C_2T_x$ MXene can reduce $CoCl_2$ and $NiCl_2$ to Co and Ni metal, while maintaining its structure, electronic conductivity, and resulting film morphology. Using nano-XRF, we find that the Co and Ni are uniformly distributed across the MXene flakes, but future studies are required to identify the specific location of the Ni and Co atoms with respect to the MXene lattice. The Co and Ni incorporation results in a 57× and 11× enhancement, respectively, of the magnetic susceptibility at room temperature, which can be utilized for applications such as electromagnetic energy absorption.

Experimental section

Material synthesis

Pristine $Ti_3C_2T_x$ MXene was prepared by selective etching of Al from Ti_3AlC_2 MAX (<40 μm, Carbon-Ukraine). Briefly, 1 g of Ti_3AlC_2 was added to a solution of 30% hydrofluoric acid (48–50%, Acros Organics) and stirred for 3 hours at 35 °C. The resulting dispersion was washed with DI water through a series of centrifugation (2500 RCF for 3 min) and decantation cycles until the supernatant reached a pH > 6. Delaminated d-$Ti_3C_2T_x$ MXene was prepared by exfoliation of multilayered ml-$Ti_3C_2T_x$ using tetramethylammonium hydroxide (TMAOH). Briefly, 3 mL of 25 wt% TMAOH solution was added to a dispersion of 1 g ml-$Ti_3C_2T_x$ in 20 mL of DI water, followed by stirring for 20 hours at 35 °C. The resulting dispersion was washed with DI water through a series of centrifugation (12,000 RCF for 5 min) and decantation cycles until the supernatant reached a pH < 8. Stock solutions of the metal salts were prepared by dissolving 0.2 g of $NiCl_2 \cdot 6H_2O$ (Acros Organics, CAS#7791-20-0) and 0.156 g of anhydrous $CoCl_2$ (Alfa Aesar, CAS#7646-79-9) in 35 mL of DI water, respectively. The salt solutions were respectively added to 5 mL (~2 mg mL^{-1}) of d-$Ti_3C_2T_x$ dispersions and mixed for 15 min at room temperature. The resulting dispersions were washed with DI water through a series of centrifugation (12 000 RCF for 5 min), mechanical shaking (5 min), and decantation cycles until the color became transparent from the initial purple ($CoCl_2$) or green ($NiCl_2$) colors. The washing process continued until the MXene flakes were well dispersed. Free-standing Co-$Ti_3C_2T_x$ and Ni-$Ti_3C_2T_x$ films were prepared by vacuum-assisted filtration through a porous polypropylene membrane (Celgard, 3501). The films were dried in a vacuum desiccator at room temperature for over 48 hours before characterization.

Materials characterization

For XPS analysis, free-standing MXene films were mounted on conductive carbon tape and measured using a PHI VersaProbe 5000 spectrometer (Physical Electronics) with a 200 μm, 50 W monochromatic Al K$_\alpha$ X-ray source. Samples were sputtered using Ar$^+$ ions for 1 min at 2 kV and 2 μA across a 2 × 2 mm area. The pass energy and step size were set at 23.5 eV and 0.05 eV, respectively. Curve fitting and quantification were conducted using the CasaXPS V2.3.19 software. SEM analysis was performed using a Zeiss Supra 50VP microscope operating at 3 kV accelerating voltage in secondary electron mode. XRD patterns were collected using a Rigaku SmartLab diffractometer (Rigaku Co. Ltd) with a Cu K$_\alpha$ source operating at 40 kV and 15 mA, within the 2θ range of 3° to 60°, at 1° min^{-1}, in 0.02° steps. Raman spectra were collected using a Renishaw InVia confocal Raman microscope using a 785 nm laser at 5% power (~0.15 mW). Magnetometry measurements were carried out using vibrating sample magnetometry in a Physical Property Measurement System (Quantum Design). For XRF mapping measurements, we used a nanofocused X-ray beam of size ~40 nm at 8.4 keV, produced by a Fresnel zone plate with an outermost zone width of 30 nm.[50,63] The XRF spectra were fitted using PyXRF software to generate elemental intensity maps.[51]

Author contributions

Material synthesis was carried out by YY and MA. YY carried out XRD, XPS, resistivity, and magnetometry measurements. MS performed SEM and EDS. RW carried out Raman spectroscopy measurements and analysis. AP, XH, and YSC contributed to the nano-XRF measurements and data analysis. YG and SJM helped to conceptualize and supervised the project. All authors have contributed to the preparation of the manuscript and given approval to the final version of the manuscript.

Conflicts of interest

The authors have no conflicts to disclose.

Acknowledgements

References

1 M. Naguib, M. Kurtoglu, V. Presser, J. Lu, J. Niu, M. Heon, L. Hultman, Y. Gogotsi and M. W. Barsoum, *Adv. Mater.*, 2011, **23**, 4248–4253.

2 V. Kamysbayev, A. S. Filatov, H. Hu, X. Rui, F. Lagunas, D. Wang, R. F. Klie and D. V. Talapin, *Science*, 2020, **369**, 979–983.

3 Y. Li, H. Shao, Z. Lin, J. Lu, L. Liu, B. Duployer, P. O. Å. Persson, P. Eklund, L. Hultman, M. Li, K. Chen, X.-H. Zha, S. Du, P. Rozier, Z. Chai, E. Raymundo-Piñero, P.-L. Taberna, P. Simon and Q. Huang, *Nat. Mater.*, 2020, **19**, 894–899.

4 A. VahidMohammadi, J. Rosen and Y. Gogotsi, *Science*, 2021, **372**, eabf1581.

5 V. Shukla, *Mater. Adv.*, 2020, **1**, 3104–3121.

6 Y. Yue, *J. Magn. Magn. Mater.*, 2017, **434**, 164–168.

7 L. Dong, H. Kumar, B. Anasori, Y. Gogotsi and V. B. Shenoy, *J. Phys. Chem. Lett.*, 2017, **8**, 422–428.

8 B. Anasori, Y. Xie, M. Beidaghi, J. Lu, B. C. Hosler, L. Hultman, P. R. C. Kent, Y. Gogotsi and M. W. Barsoum, *ACS Nano*, 2015, **9**, 9507.

9 B. Anasori, C. Shi, E. J. Moon, Y. Xie, C. A. Voigt, P. R. Kent, S. J. May, S. J. Billinge, M. W. Barsoum and Y. Gogotsi, *Nanoscale Horiz.*, 2016, **1**, 227–234.

10 J. Yang, X. Zhou, X. Luo, S. Zhang and L. Chen, *Appl. Phys. Lett.*, 2016, **109**, 203109.

11 W. Sun, Y. Xie and P. R. C. Kent, *Nanoscale*, 2018, **10**, 11962–11968.

12 S. Li, J. He, L. Grajciar and P. Nachtigall, *J. Mater. Chem. C*, 2021, **9**, 11132–11141.

13 N. C. Frey, A. Bandyopadhyay, H. Kumar, B. Anasori, Y. Gogotsi and V. B. Shenoy, *ACS Nano*, 2019, **13**, 2831–2839.

14 J. Yang, S. Zhang, A. Wang, R. Wang, C.-K. Wang, G.-P. Zhang and L. Chen, *Nanoscale*, 2018, **10**, 19492–19497.

15 Q. Tang, Z. Zhou and P. Shen, *J. Am. Chem. Soc.*, 2012, **134**, 16909–16916.

16 M. Zhao, J. Chen, S.-S. Wang, M. An and S. Dong, *Phys. Rev. Mater.*, 2021, **5**, 094408.

17 R. Ponce-Pérez, J. Guerrero-Sanchez, S. J. Gutierrez-Ojeda and M. G. Moreno-Armenta, *ACS Appl. Electron. Mater.*, 2021, **3**, 4967–4976.

18 Y. Yue, B. Wang, N. Miao, C. Jiang, H. Lu, B. Zhang, Y. Wu, J. Ren and M. Wang, *Ceram. Int.*, 2021, **47**, 2367–2373.

19 J. Yang, X. Luo, X. Zhou, S. Zhang, J. Liu, Y. Xie, L. Lv and L. Chen, *Comput. Mater. Sci.*, 2017, **139**, 313–319.

20 J. He, G. Ding, C. Zhong, S. Li, D. Li and G. Zhang, *Nanoscale*, 2019, **11**, 356–364.

21 M. W. Barsoum, *Prog. Solid State Chem.*, 2000, **28**, 201–281.

22 M. Sokol, V. Natu, S. Kota and M. W. Barsoum, *Trends Chem.*, 2019, **1**, 210–223.

23 C. Si, J. Zhou and Z. Sun, *ACS Appl. Mater. Interfaces*, 2015, **7**, 17510–17515.

24 M. Je, Y. Lee and Y.-C. Chung, *Thin Solid Films*, 2016, **619**, 131–136.

25 Q. Sun, Z. Fu and Z. Yang, *J. Magn. Magn. Mater.*, 2020, **514**, 167141.

26 X. Feng, Z. He, R. Peng, Y. Dai, B. Huang and Y. Ma, *Phys. Rev. Mater.*, 2022, **6**, 044001.

27 M. Jaouen, M. Bugnet, N. Jaouen, P. Ohresser, V. Mauchamp, T. Cabioc'h and A. Rogalev, *J. Phys.: Condens. Matter*, 2014, **26**, 176002.

28 O. Akinola, I. Chakraborty, H. Celio, D. Akinwande and J. A. C. Incorvia, *J. Mater. Res.*, 2021, **36**, 1980–1989.

29 Y. Zhang, Z. Cui, B. Sa, N. Miao, J. Zhou and Z. Sun, *Nanoscale Horiz.*, 2022, **7**, 276–287.

30 K. Hantanasirisakul, B. Anasori, S. Nemsak, J. L. Hart, J. Wu, Y. Yang, R. V. Chopdekar, P. Shafer, A. F. May, E. J. Moon, J. Zhou, Q. Zhang, M. L. Taheri, S. J. May and Y. Gogotsi, *Nanoscale Horiz.*, 2020, **5**, 1557–1565.

31 P. Liu, V. M. H. Ng, Z. Yao, J. Zhou and L. B. Kong, *Mater. Lett.*, 2018, **229**, 286–289.

32 X. Li, W. You, L. Wang, J. Liu, Z. Wu, K. Pei, Y. Li and R. Che, *ACS Appl. Mater. Interfaces*, 2019, **11**, 44536–44544.

33 J. He, D. Shan, S. Yan, H. Luo, C. Cao and Y. Peng, *J. Magn. Magn. Mater.*, 2019, **492**, 165639.

34 Q. Zhang, D. Xu, Y. Si, R. Xu, B. Luo, S. He and D. Liu, *ACS Appl. Nano Mater.*, 2022, **5**, 7175–7186.

35 X. Li, M. Zhang, W. You, K. Pei, Q. Zeng, Q. Han, Y. Li, H. Cao, X. Liu and R. Che, *ACS Appl. Mater. Interfaces*, 2020, **12**, 18138–18147.

36 Y. Cui, Z. Liu, Y. Zhang, P. Liu, M. Ahmad, Q. Zhang and B. Zhang, *Carbon*, 2021, **181**, 58–68.

37 L. Liang, G. Han, Y. Li, B. Zhao, B. Zhou, Y. Feng, J. Ma, Y. Wang, R. Zhang and C. Liu, *ACS Appl. Mater. Interfaces*, 2019, **11**, 25399–25409.

38 N. Li, X. Xie, H. Lu, B. Fan, X. Wang, B. Zhao, R. Zhang and R. Yang, *Ceram. Int.*, 2019, **45**, 22880–22888.

39 L. Liang, R. Yang, G. Han, Y. Feng, B. Zhao, R. Zhang, Y. Wang and C. Liu, *ACS Appl. Mater. Interfaces*, 2020, **12**, 2644–2654.

40 Y. Peng, L. Deng, H. Luo and S. Huang, *Results Phys.*, 2020, **19**, 103516.

41 J. He, X. Liu, Y. Deng, Y. Peng, L. Deng, H. Luo, C. Cheng and S. Yan, *J. Alloys Compd.*, 2021, **862**, 158684.

42 X. Li, Z. Wu, W. You, L. Yang and R. Che, *Nano-Micro Lett.*, 2022, **14**, 73.

43 C. Wen, X. Li, R. Zhang, C. Xu, W. You, Z. Liu, B. Zhao and R. Che, *ACS Nano*, 2022, **16**, 1150–1159.

44 C. Zhou, X. Wang, H. Luo, L. Deng, S. Wang, S. Wei, Y. Zheng, Q. Jia and J. Liu, *Appl. Surf. Sci.*, 2019, **494**, 540–550.

45 H. Liang, G. Chen, D. Liu, Z. Li, S. Hui, J. Yun, L. Zhang and H. Wu, *Adv. Funct. Mater.*, 2023, **33**, 2212604.

46 H. Liu, X. Li, X. Zhao, M. Zhang, X. Liu, S. Yang, H. Wu and Z. Ma, *Adv. Funct. Mater.*, 2023, **33**, 2304442.

47 H. Jin, K. Wang, Z. Mao, L. Tang, J. Zhang and X. Chen, *J. Phys.: Condens. Matter*, 2022, **34**, 015701.

48 W. Feng, H. Luo, S. Zeng, C. Chen, L. Deng, Y. Tan, X. Zhou, S. Peng and H. Zhang, *Mater. Chem. Front.*, 2018, **2**, 2320–2326.

49 M. W. Hakim, S. Fatima, R. Tahir, M. Z. Iqbal, H. Li and S. Rizwan, *J. Energy Storage*, 2023, **61**, 106662.

50 E. Nazaretski, H. Yan, K. Lauer, N. Bouet, X. Huang, W. Xu, J. Zhou, D. Shu, Y. Hwu and Y. S. Chu, *J. Synchrotron Radiat.*, 2017, **24**, 1113–1119.

51 L. Li, Y. Hanfei, X. Wei, Y. Dantong, H. Annie, L. Wah-Keat, I. C. Stuart and S. C. Yong, In PyXRF: Python-based X-ray fluorescence analysis package, Proc. SPIE 10389, X-Ray Nanoimaging: Instruments and Methods III, 2017, p. 103890U.

52 M. C. Biesinger, B. P. Payne, A. P. Grosvenor, L. W. M. Lau, A. R. Gerson and R. S. C. Smart, *Appl. Surf. Sci.*, 2011, **257**, 2717–2730.

53 Y. Long, Y. Tao, T. Shang, H. Yang, Z. Sun, W. Chen and Q.-H. Yang, *Adv. Sci.*, 2022, **9**, 2200296.

54 L. Wang, H. Song, L. Yuan, Z. Li, Y. Zhang, J. K. Gibson, L. Zheng, Z. Chai and W. Shi, *Environ. Sci. Technol.*, 2018, **52**, 10748–10756.

55 Y. Yi, Y. Ma, F. Ai, Y. Xia, H. Lin and G. Zhu, *Chem. Commun.*, 2021, **57**, 7790–7793.

56 W. Peng, M. Luo, X. Xu, K. Jiang, M. Peng, D. Chen, T.-S. Chan and Y. Tan, *Adv. Energy Mater.*, 2020, **10**, 2001364.

57 H. Gu, X. Li, J. Zhang and W. Chen, *Small*, 2022, **18**, 2105883.

58 K. Eid, Q. Lu, S. Abdel-Azeim, A. Soliman, A. M. Abdullah, A. M. Abdelgwad, R. P. Forbes, K. I. Ozoemena, R. S. Varma and M. F. Shibl, *J. Mater. Chem. A*, 2022, **10**, 1965.

59 A. Sarycheva and Y. Gogotsi, *Chem. Mater.*, 2020, **32**, 3480–3488.

60 "Magnetic Data Storage", in *Magnetic Materials: Fundamentals and Applications*, ed. N. A. Spaldin, Cambridge University Press, Cambridge, 2nd edn, 2010, pp. 177–188.

61 C. Binns, in *Frontiers of Nanoscience*, ed. C. Binns, Elsevier, 2014, vol. 6, pp. 1–32.

62 D. X. Chen, A. Sanchez, E. Taboada, A. Roig, N. Sun and H. C. Gu, *J. Appl. Phys.*, 2009, **105**, 083924.

63 H. Yan, N. Bouet, J. Zhou, X. Huang, E. Nazaretski, W. Xu, A. P. Cocco, W. K. S. Chiu, K. S. Brinkman and Y. S. Chu, *Nano Futures*, 2018, **2**, 011001.